Ultrafast Heat Transfer at the Nanoscale: Controlling Heat Anisotropy

Jean-François Bryche, Marlo Vega, Julien Moreau, Paul-Ludovic Karsenti, Paul Bresson, Mondher Besbes, Philippe Gogol, Denis Morris, Paul G Charette, Michael Canva

Ultrafast Heat Transfer at the Nanoscale: Controlling Heat Anisotropy

JEAN-FRANÇOIS BRYCHE[1,2,3†*], MARLO VEGA[1,2,4†], JULIEN MOREAU[4], PAUL-LUDOVIC KARSENTI[3], PAUL BRESSON[1,2,4], MONDHER BESBES[4], PHILIPPE GOGOL[1,2,5], DENIS MORRIS[1,2,3], PAUL G. CHARETTE[1,2] AND MICHAEL CANVA[1,2]

[1] Laboratoire Nanotechnologies Nanosystèmes (LN2), CNRS, Université de Sherbrooke - J1K 0A5 Sherbrooke, QC, Canada.
[2] Institut Interdisciplinaire d'Innovation Technologique (3IT), Université de Sherbrooke - J1K 0A5 Sherbrooke, QC, Canada
[3] Faculté des Sciences, Université de Sherbrooke - J1K 2R1 Sherbrooke, QC, Canada.
[4] Université Paris-Saclay, Institut d'Optique Graduate School, CNRS, Laboratoire Charles Fabry - 91127 Palaiseau, France.
[5] Centre de Nanosciences et de Nanotechnologies, Université Paris-Saclay, CNRS - 91120 Palaiseau, France.

*Corresponding author: jean-francois.bryche@cnrs.fr

†J-F.B. and M.V contributed equally to this paper (shared first authorship).

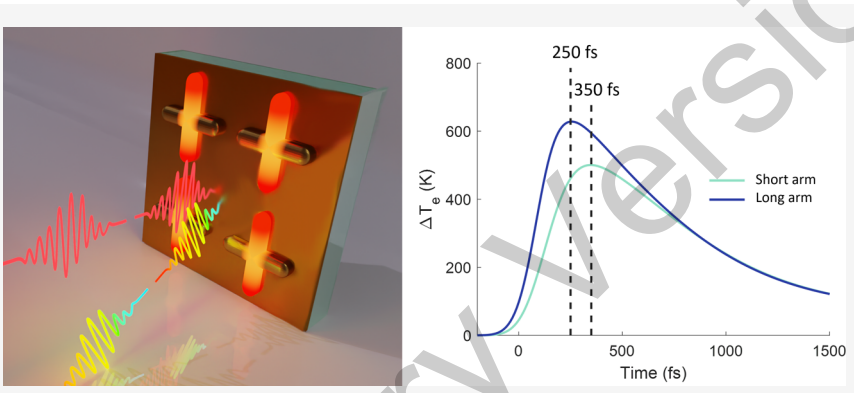

ABSTRACT: Thermoplasmonics has benefited from increasing attention in recent years by exploiting the photothermal effects within plasmonic nanoparticles to generate nanoscale heat sources. Recently, it has been demonstrated that exciting gold nanoparticles with ultrashort light pulses could be used to achieve high-speed light management and nanoscale heat-sensitive chemical reaction control. In this work, we study non-uniform thermal energy transient distribution inside cross-shaped nanostructures with femtosecond transient spectroscopy coupled to a thermo-optical numerical model, free of fitting parameters. We show experimentally and numerically that the polarization of the excitation light can control the heat distribution in the nanostructures. We also demonstrate the necessity of considering nonthermal electron ballistic displacement in fast transient heat dynamics models.

KEYWORDS: *ultrafast spectroscopy, pump−probe experiments, plasmonics, hot carrier dynamics*

INTRODUCTION

By absorbing and converting light into heat, metal nanoparticles behave as sub-micrometer sources of heat that could find use in fields such as nanomedicine,[1] photovoltaics,[2] and photochemistry,[3−5] especially with high temperatures and heat confinement that can be achieved with femtosecond pulsed illumination.[6] However, this regime is challenging to study both theoretically and experimentally, and much remains to be fully understood. The heat dynamics of nanoparticles following femtosecond excitation are a nonlinear combination of processes happening on very different time scales.[7−9] Light absorption first generates out-of-equilibrium electrons (called non-thermal or "hot" electrons) that thermalize in a Fermi−Dirac distribution in a few hundred femtoseconds by electron−electron scattering, where the electron temperature reaches hundreds to thousands of degrees while the lattice remains cold. The electrons then thermalize with the lattice on a picosecond timescale, increasing the lattice temperature by only a few degrees due to its high thermal capacity. Heat finally disperses into the local environment via phonon−phonon diffusion on a nanosecond timescale.[10]

Thermal relaxation in thin metal films has been studied to various degrees of complexity.[7,11−13] In studies pertaining to nanostructured surfaces, the temperature distribution inside nanostructures is generally considered to be uniform. However, this assumption is not valid for heat dynamics at very short time scales (<1 ps).[14] In the early stages of heating, non-thermal electron energy density, lattice temperature, and electronic temperature can be highly heterogeneous due to anisotropic surface absorption.[15] Furthermore, non-thermal electrons are usually considered static (unmoving) in numerical simulations. However, in nanosized objects, non-

Received: December 15, 2022

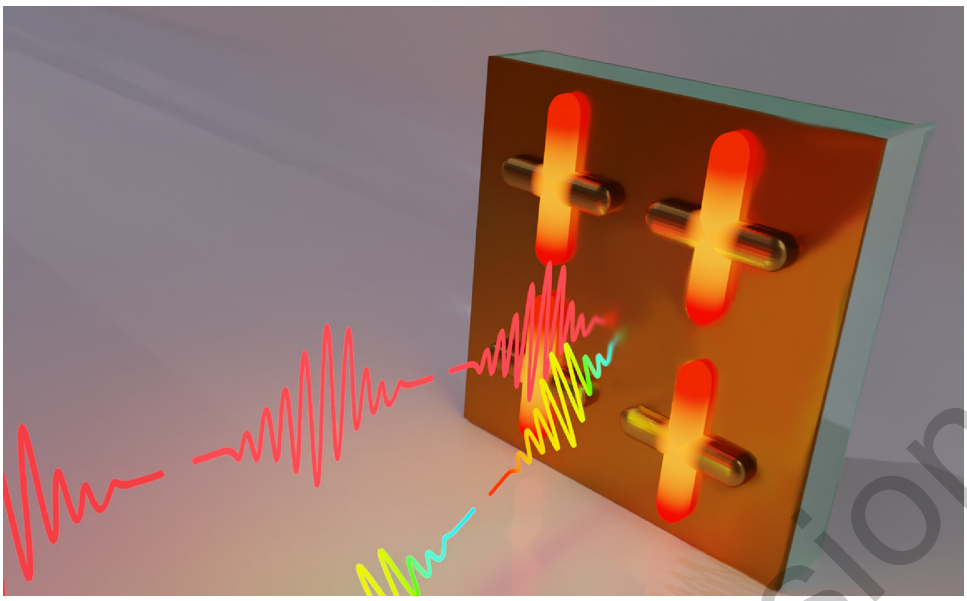

Figure 1. Illustration of the selective heating of one arm of the nanocrosses.

thermal electrons travel ballistically (i.e., without interaction over relatively long distances compared to the characteristic size of the medium) at speeds close to the Fermi velocity.[16,17] Thus, ballistic electrons modify the non-thermal energy distribution and heat profile at the nanoscale. These phenomena must therefore be accounted for in accurate modeling of heat dynamics in nanostructured metal surfaces at short time scales. An improved understanding of these phenomena could lead to the design of original approaches for the development of new applications. For example, recent works have shown that anisotropic heating at small scales can be used for high-speed light management,[14,18−20] optimization of nanoreactors for photothermal chemistry,[21] and control of chemical reactions at the nanoscale.[22,23]

In this work, we studied the time-dependent spatial distribution of non-thermal electron energy density, electronic temperature, and lattice temperature in an array of asymmetric gold nanocrosses under femtosecond pulsed illumination. Time-resolved temperature distributions at the nanoscale were estimated with a thermo-optical numerical model that includes non-thermal electron ballistic displacement. Modeling results were validated against experimental measurements acquired with a femtosecond pump−probe spectroscopy system. The nanocrosses have distinct longitudinal plasmonic resonances along each intersecting arm. Consequently, by tuning the pump beam polarization and wavelength to the desired optical response, one can selectively heat either of the two arms (see Figure 1). Heat and non-thermal energy are then carried to the other arm by thermal diffusion and electron ballistic displacement. The results presented below demonstrate how the heat dynamics in the arms of the asymmetric crosses were determined and how the heat distribution can be controlled at the nanoscale. We highlight the significant impact of non-thermal ballistic electron propagation on the anisotropic heating of the nanostructures.

NUMERICAL MODEL

Historically, a "2-temperature model" (2TM) has been used to describe transient heat relaxation in metals. The 2TM consists in solving a set of two coupled differential equations involving the electronic temperature (T_e) and the lattice temperature (T_l). The 2TM is based on the hypothesis that non-thermal electrons are instantaneously thermalized, which does not agree with experimental observations.[13,24] To consider non-thermal electrons, a "3-temperature model" (3TM), where the third "temperature" refers to the non-thermal electron energy density (N), was introduced by Sun *et al.*[13]

The numerical modeling results shown below were generated with a hybrid electromagnetic model based on the finite element method (FEM) and the Fourier modal method,[25] which enables faster calculations over geometry with features at different scale levels. The model[26] is based on the 3TM but takes into consideration non-thermal electron ballistic displacement inside the nanostructures. This is justified by the fact that the ballistic electron velocity is close to the Fermi velocity,[17] which is around 1.4 nm/fs for gold.[27] With a mean lifetime of ∼260 fs,[28] non-thermal electrons travel around 360 nm before interacting, a distance greater than the size of typical nanostructures. It should be noted that the non-thermal propagation of electrons has also been considered by using a standard heat diffusion term.[29]

In the numerical computations, the temporal dynamics of N, T_e, and T_l following a pump pulse are calculated in each FE cell with the set of coupled equations detailed in the Supporting Information. The resulting temperature-dependent metal permittivities due to intraband and interband transitions are then calculated over time with the Drude[30] and Rosei[31−34] models, respectively. The model can then estimate the transient transmissivity and reflectivity responses of the nanostructured surface at any given time by injecting the time-resolved metal permittivity of each element back into the FE model. No ad-hoc non-physical parameters are used to improve the fits to the experimental results. The model incorporates room temperature metal permittivity values that were measured by ellipsometry on a 300 nm-thick gold film deposited under the same conditions as the nanostructured films (see the Supporting Information).

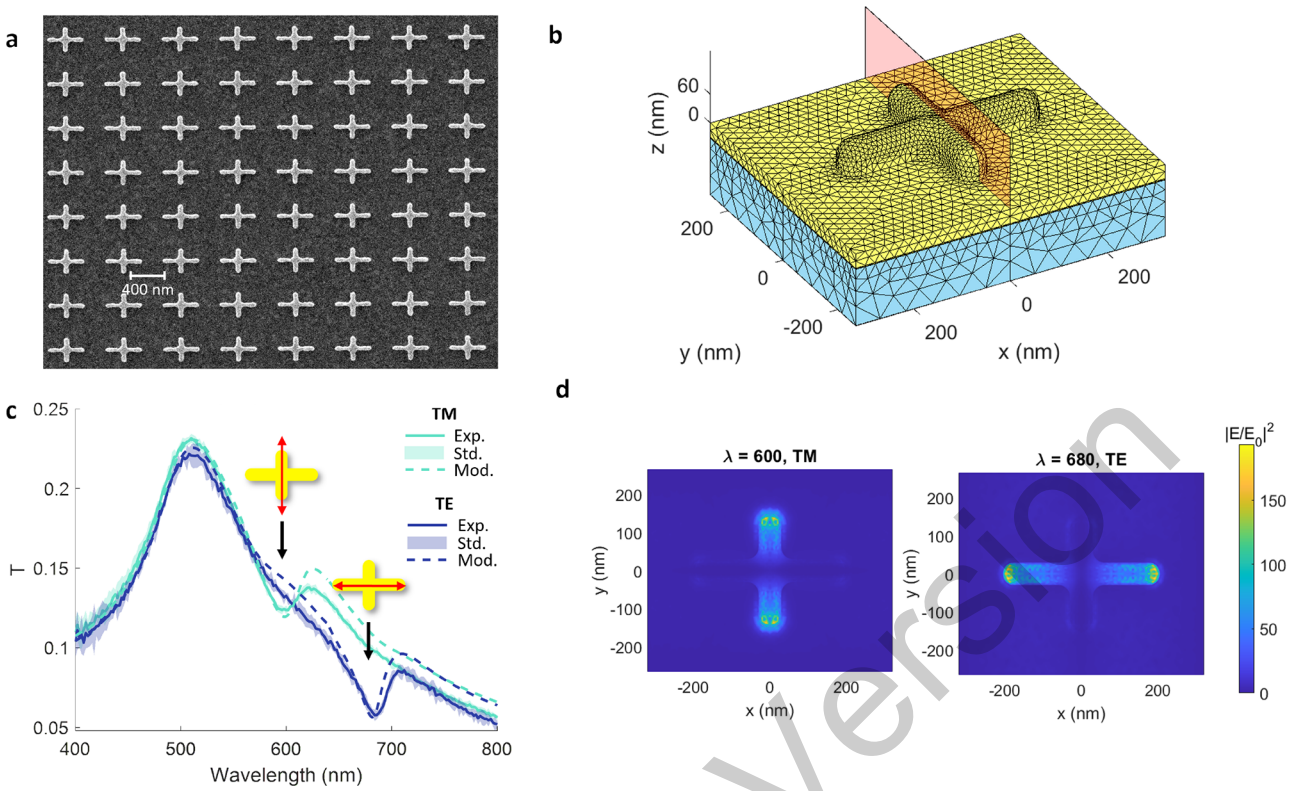

Figure 2. (a) SEM image of a gold nanocross array. (b) Unit cell geometry and mesh used for numerical modeling. The pump−probe beam incidence plane is colored in red. (c) Experimental (solid lines) and modeled (dashed lines) steady-state transmission spectra through the array at normal incidence for both polarizations. The arrows indicate the transmission minima at resonance for each arm in the cross. The standard deviation with a 95% confidence interval over six spectra is represented in a lighter color for each curve. (d) Profiles of the electric field amplitude squared at the metal surface for the two resonance wavelengths (E0 is the incident electric field amplitude).

EXPERIMENTAL RESULTS

Arrays of 60 nm-thick gold nanocrosses were fabricated by e-beam lithography atop 30 nm-thick gold films with a 2.5 nm titanium adhesion layer on a BK7 glass substrate. The fabrication process is detailed in the Methods Section. Figure 2a shows a SEM image of a fabricated array. The dimensions of the crosses are 300/410 nm lengths, 60 nm height, 60 nm width, and 530/640 nm center-to-center period along the short/long arm axes. TM/TE polarization directions are defined by the orientation of the electric field vector parallel/normal to the pump−probe plane of incidence (colored in red in Figure 2b). Note that the geometry of the arm extremities and the center of the crosses of the unit cell were modeled as 30 nm radius spherical shapes (Figure 2b) to better reproduce the actual shape of fabricated samples measured by AFM (see the Supporting Information), which improved the fit to the measured spectra.

To characterize the localized surface plasmon resonances (LSPR) in each nanocross arm, we performed spectrally resolved transmission measurements in the steady-state regime. Figure 2c shows the measured and modeled transmission spectra for the illuminated nanocross array at normal incidence for the two orthogonal polarizations. The spectra show LSPR absorption bands around 600 nm for the TM polarization (electric field polarized along the short arm) and 680 nm for the TE polarization (electric field polarized along the long arm), in good agreement with the model. Figure 2d shows the modeling results for the electric field amplitude squared $|E/E_0|^2$ at the metal surface, normalized by the magnitude of the incident excitation field, $|E_0|$. For both wavelengths, field strength is highest at the extremity of the arm in which the resonance is excited (parallel to the incident electric field). Because the absorbed power is proportional to the square of the electric field,[9,26] the modeling results indicate that absorption is expected to be over two orders of magnitude higher at the extremities of the excited arms relative to the perpendicular non-excited arms (Figure 2d). Therefore, by exciting either of the two modes of Figure 2d, one can selectively heat the extremity of a single arm of the nanocross, generating transient inhomogeneous thermal energy distribution at ultrashort time scales.

To study the heat dynamics in the nanostructures, we performed reflectivity measurements in the transient regime with the pump−probe setup described in a previous work[26] and briefly detailed in the Methods Section. Due to the presence of the gold film under the nanostructures, measurements were performed in reflection to obtain a better signal-to-noise ratio. Pump and probe beams were angled at 7.5 and 6.5° from normal incidence, respectively, due to experimental constraints. Figure 3a,b shows the measured time- and wavelength-resolved maps of normalized reflectivity variation $\Delta R/R$, resulting from the excitation of the TE LSPR mode in the long arm by a TE-polarized pump pulse centered at 677 nm, where ΔR is the difference in reflectivity from the steady-state value, R, as a function of wavelength. The vertical axis in the maps indicates the delay between the pump heating pulse and the probe measurement pulse. The transient optical response from the long arm, directly excited by the pump, was measured with a TE-polarized probe (Figure 3a). The transient

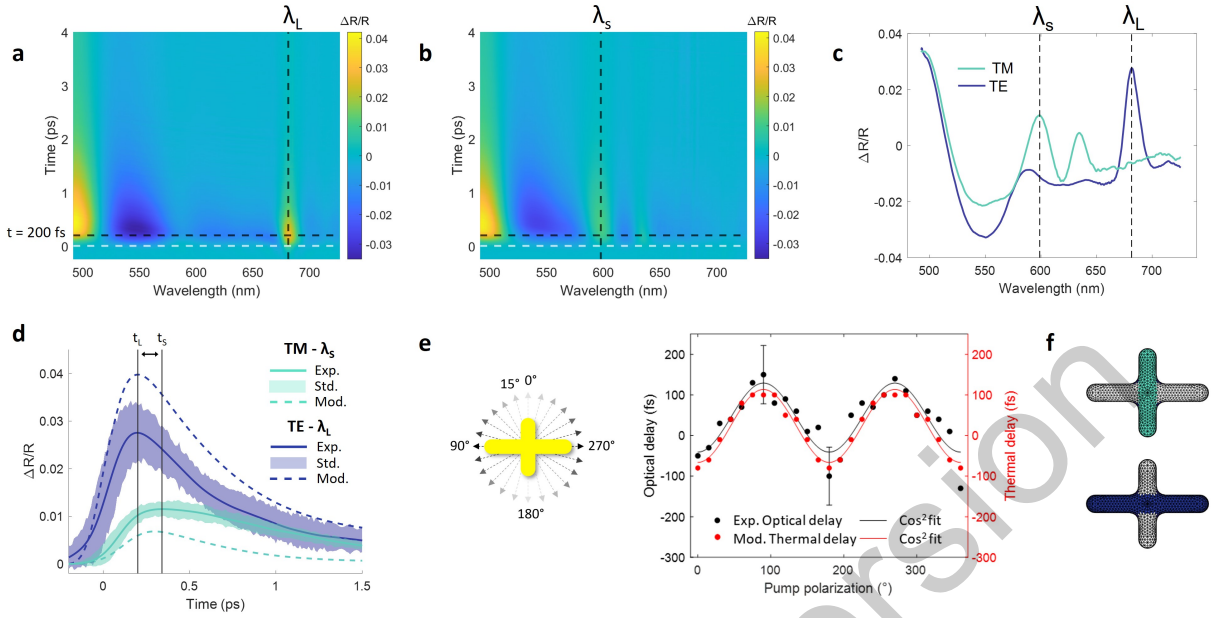

Figure 3. Experimental measurements of transient normalized reflectivity change as a function of time and wavelength resulting from the excitation of the TE LSPR mode in the long arm by a TE-polarized pump pulse centered at 677 nm for (a) TE and (b) TM probe beams (ΔR is the difference in reflectivity from the steady-state value, R, as a function of wavelength). The fluence is 5.6 J/m^{-2}. The vertical time axis indicates the delay between the pump heating pulse and the probe measurement pulse. λ_S and λ_L are the wavelengths at which the maximum $\Delta R/R$ values are reached for the TE and TM LSPR modes, respectively. The black and white dashed lines indicate time delays of 0 and 200 fs, respectively. (c) Transient reflectivity change spectra as a function of wavelength from (a) and (b) at a 200 fs delay. (d) Measured (solid) and modeled (dashed lines) normalized reflectivity change as a function of time delay at λ_S and λ_L. The standard deviation over 10 measurement is shown in a lighter color for each curve. (e) Measured optical delay (red dots) and modeled thermal delay (black dots) as a function of pump polarization angle (pump polarization with respect to cross orientation shown on the left). A cos^2 model is fitted for each (red and black continuous curves) for ease of visualization. The error bars for the time delay are shown for 90 and 180° pump polarization angles. Uncertainty calculations are detailed in the Supporting Information. (f) Finite element meshing of the geometry for the time delay calculations. Turquoise and blue colors show the mesh elements used to calculate the mean temperature of the short and long arms, respectively.

optical response from the short arm, resulting from heat transfer from the long arm, was measured with a TM-polarized probe pulse (Figure 3b). For both maps, the group velocity dispersion of the probe beam was numerically corrected with the procedure detailed by Ruckebusch *et al.*[35] The relative "0" time is thus the same for all wavelengths.

Figure 3c shows the measured TE and TM reflectivity change spectra as a function of wavelength for a delay of 200 fs (horizontal black dashed lines in Figure 3a,b). The characteristic profile for gold interband transitions is visible from 490 nm to over 550 nm for both polarizations. The TE peak at $\lambda_L \approx 680$ nm corresponds to the "bleaching" of the LSPR mode[24,36] along the long arm of the nanocrosses, which is related to the generation of non-thermal electrons and associated local increase in the electronic temperature. Similarly, the TM peak at $\lambda_S \approx 598$ nm corresponds to the bleaching of the LSPR mode along the short arm. A second peak appears in Figure 3c for the TM polarization corresponding to a mode that we could not identify (it is only visible for non-normal excitation angles and therefore does not appear in Figure 2c).

Figure 3d shows the plots of measured and modeled time-resolved reflectivity changes at λ_S and λ_L (the LSPR resonance peaks for the short and long arms), illustrating the distinctive dynamics of the two optical responses. The measured reflectivity change from the long arm (λ_L) is over a factor of two higher than that from the short arm due to direct heating by the pump. Furthermore, the response for λ_S is delayed relative to λ_L due to indirect vs direct heating, where the measured time delay, $t_S - t_L$, between the two maxima (black vertical lines in the inset of Figure 3d) is 140 ± 50 fs (uncertainty calculations are detailed in the Supporting Information) compared to 100 fs predicted by the model, i.e., within measurement error. Although the modeled $\Delta R/R$ values at λ_L are higher than the measurements and lower at λ_S, the overall behavior over time in both cases is well reproduced by the model. The origin of the differences between modeling and experimental results is discussed in the Supporting Information.

Figure 3e shows the measured time delay as a function of the pump polarization angle fitted with a cos^2 law for ease of visualization. The delay maxima are reached for 90 and 270° pump polarization angles, i.e., when the electric field is fully resonant with the long arm. Moving away from these angles, the time delay decreases progressively, cancels, and then reverses when the pump is polarized along the short arm. These results are consistent with the locations of the absorption hot spots on the arms of the crosses shown in Figure 2d as a function of the pump polarization angle. To further demonstrate the link between the measured optical delay and the thermalization in the two arms, we used our model to calculate the "thermal delay" defined as $t_{Th-S} - t_{Th-L}$, where t_{Th-S} and t_{Th-L} are the times at which the maximum T_e values are reached in the short and long arms,

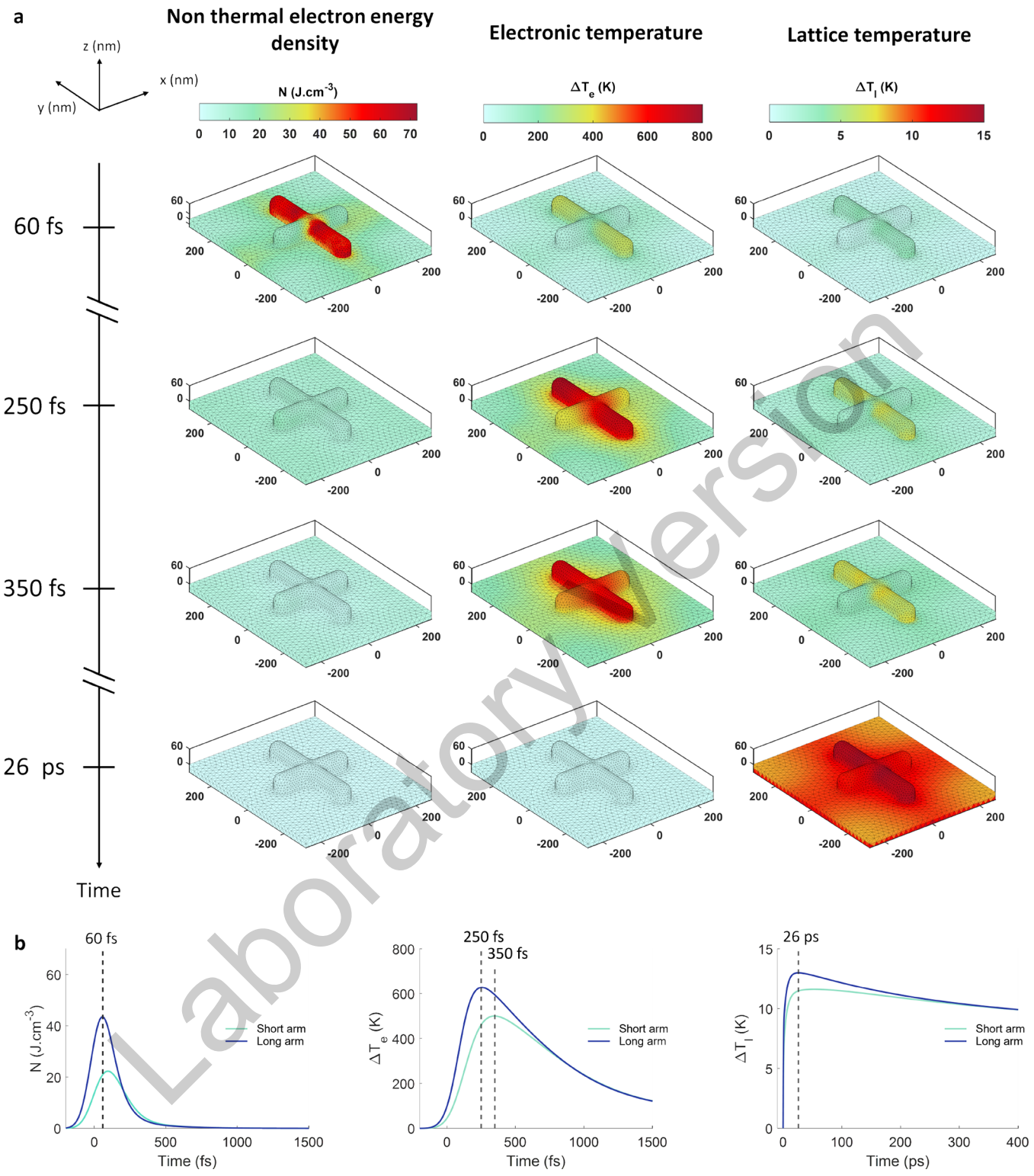

Figure 4. (a) Transient spatial distribution modeling results of non-thermal electron energy density N (left column), electronic temperature variation ΔT_e (middle column), and lattice temperature variation ΔT_l (right column) at four different times. The pump at 677 nm is polarized along the long arm direction with a fluence of 5.6 J/m^{-2}. The chosen times of 60 fs, 240 fs, 340 fs, and 26 ps are, respectively, the time at which N is maximum in the long arm, T_e is maximum in the long arm, T_e is maximum in the small arm, and T_l is maximum in the long arm. (b) Mean values of N, T_e, and T_l of the long (blue curve) and short (green curve) arms of the nanostructure as a function of time (note the different time scales).

respectively. Figure 3f shows the FE model elements used to calculate the mean electronic temperatures in the short and long arms. The modeled thermal delays are compared to the measured optical delays (see Figure 3e). The curves are in excellent agreement, demonstrating that the optical delay is a reliable experimental indicator of heat anisotropy in the experiments. For a polarization angle of approximately 30°, the short and long arms are heated equivalently, and the resulting

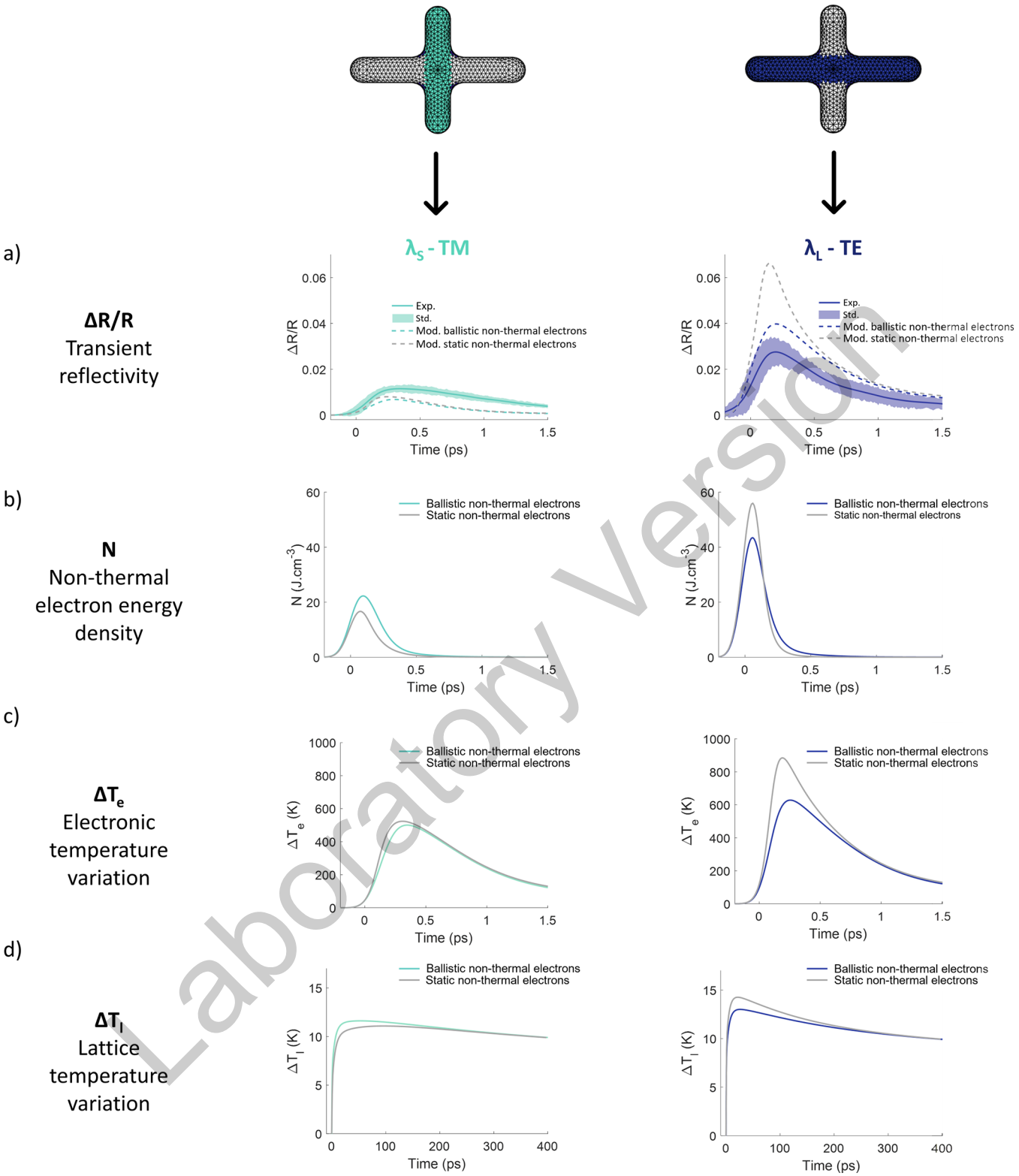

Figure 5. (a) Transient reflectivity at λ_S (left graph) and λ_L (right graph) following a pump pulse. (b) Non-thermal electron energy density, (c) electronic temperature variation, and (d) lattice temperature variation as a function of time in the short (left column) and long arms (right column). For each row, the modeling results assuming static non-thermal electrons are shown in gray for comparison with the results from our model that involves ballistic non-thermal electrons.

delay is close to nil. This angle is in accordance with the angle for which the absorption is equal in the two arms (see the Supporting Information). As the pump TE component is more efficiently absorbed (resonant condition), homogeneous absorption (null delay) between the two arms is reached when the TM component of the electric field is dominant. This also explains why the curves are not centered at y = 0 fs but slightly shifted upward. Overall, these results demonstrate that

pump polarization angle can be used to control the heat inhomogeneity in the arms in the nanocrosses.

DISCUSSION

Figure 4a shows the modeled time-resolved surface distributions of ΔT_e and ΔT_l (variations with respect to room temperature of T_e and T_l) as well as non-thermal electron energy density N for specific times corresponding to the following: maximum N in the long arm (60 fs), maximum ΔT_e in the long arm (250 fs), maximum ΔT_e in the short arm (350 fs), and maximum ΔT_l in the long arm (26 ps). The maps show that N, T_e, and T_l rise, relax, and propagate at different time scales. Figure 4b shows the plots of the mean values of N, ΔT_e, and ΔT_l as a function of time in the long and short arms following an excitation of the LSPR mode in the long arm.

Non-thermal electrons are generated mainly in the excited arm (i.e., the long arm in this case) and thermalize mainly by electron−electron scattering in less than 300 fs. Despite the ballistic propagation of non-thermal electrons, non-thermal energy density remains relatively low in the small arm (~22 vs ~43 J·cm^{-3} in the long arm). We attribute this result to the geometry of the nanostructures: non-thermal electrons generated in the extremities of the long arm can only reach the other arm by being reflected at the gold/air and gold/titanium interfaces. The probability of non-thermal electrons reaching the small arm is thus low, resulting in a relatively low N. Non-thermal electrons thermalize therefore mainly in the long arm, increasing its electronic temperature. The long arm reaches a maximum ΔT_e of ~630 K at 250 fs, while the small arm reaches a maximum ΔT_e that is significantly lower (~500 K) at 350 fs (100 fs later). Thus, there is a maximum electronic temperature difference of 130 K between the two arms. In comparison, the dynamics of lattice temperatures are slower, and the temperature increases are ~50× smaller. This is mainly due to the high lattice heat capacity of gold. Also, as the gold lattice conductivity is lower by two to three orders of magnitude relative to the electronic conductivity, lattice temperature homogeneity in the nanostructures is only achieved ~200 ps after the absorption of the pump pulse. The maximum lattice temperature difference between the two arms is only ~1.5 K, compared to the 130 K difference in maximum electronic temperatures.

Gold cross arrays could be a convenient platform to control chemical reactions at the nanoscale whether the reaction is driven by a purely thermal process or by "hot" carriers (non-thermal electrons and holes). This type of application requires the quantitative modeling of the time-resolved nanoscale heat profile. As stated earlier, most numerical models consider that non-thermal electrons are immobile and thermalize at their generated location. Our numerical model considers that non-thermal electrons displace ballistically in the metal (nanostructures and film) and are elastically reflected at the interfaces between metallic and dielectric media. The model does not consider any privileged propagation direction (see the Supporting Information). To visualize the impact of the inclusion of non-thermal ballistic electrons in our model, Figure 5 compares the results obtained by considering non-thermal electrons as ballistic or static. Figure 5a shows the transient reflectivity at λ_L and λ_S (resonance wavelengths of the short and long arms) following a pump pulse. Removing non-thermal electron ballistic displacement does not change the delay but increases $\Delta R/R$ for both resonances: $\Delta R/R$ increases slightly at λ_S (17%) and more substantially (67%) at λ_L to reach a maximum twice the experimentally measured value. Thus, in our configuration, considering non-thermal ballistic electron displacement better reproduces the experimental measurements.

Figure 5b−d compares the N, ΔT_e, and ΔT_l time evolution in the two arms (averaged over the volumes shown in darker shades at the top of Figure 5) with and without non-thermal ballistic electron displacement. Considering the non-thermal electrons as static mainly changes the values of N and ΔT_e at very short time scales (<1 ps). At longer times, either consideration (static or ballistic) lead to the same average N and ΔT_e profiles along both arms. Removing ballistic non-thermal electron propagation decreases the N maximum value by 34% in the small arm and increases it by 28% in the long arm. This behavior is related to the non-thermal electrons being mainly generated in the long arm due to the resonant excitation of the TE LSPR. Without considering ballistic non-thermal propagation, non-thermal electrons thermalize in the long arm and do not reach the small arm. Videos of the simulated time evolution of N at the nanostructures surface with and without considering ballistic displacement are shown in the Supporting Information. Ballistic non-thermal electron propagation does not significantly change the maximum ΔT_e in the small arm (+5%) but does impact the maximum ΔT_e reached in the long arm (+41%). The ΔT_l maximum variation decreases slightly in the short arm (<5%) and increases by 10% in the long arm. Therefore, adding ballistic electron displacement to the 3TM results in a significant difference in the maximum non-thermal energy density and the electronic temperature reached, particularly in the absorption hot spots of the nanostructures.

CONCLUSIONS

In this work, we studied nanoscale heat dynamics inside an array of asymmetric gold cross-shaped nanostructures with time-resolved reflectivity measurement coupled with a thermo-optical numerical model. We selectively excited one arm with the pump beam and indirectly measured each arm's thermal response by spectrally probing the transient reflectivity at the wavelengths corresponding to their resonances. The experiments revealed a time delay between the transient reflectivity dynamics dictated by the distinct resonances in the nanocross arms, a consequence of a thermalization delay between the arms of the nanostructures. The delay and thus the heat distribution inside the nanostructures could be easily tuned by changing the pump polarization angle. Gold nanocrosses could thus be a convenient platform to control heat-sensitive chemical reactions at the nanoscale. We numerically mapped non-thermal electron energy density, electronic temperature variation, and lattice temperature variation distributions and showed that these quantities significantly differ between the two arms of the crosses. Using a modified 3-temperature model that includes non-thermal ballistic electron displacement has demonstrably improved the fit to the experimental data, clearly showing that ballistic electron displacement must be considered to better understand and model nanoscale energy propagation in nanostructures at very fast time scales.

METHODS

Sample Fabrication. The arrays of nanoparticles were fabricated using a standard electron-beam lithography-based metal lift-off process. First, the BK7 D263 glass substrate was

cleaned with three successive 5 min baths of propan-2-one, propan-2-ol, deionized water, and a 15 min bath of Piranha solution (3:1 mix of concentrated sulfuric acid (H_2SO_4)/H_2O_2). A 2.5 nm titanium adhesion layer followed by a 30 nm gold layer was deposited by e-beam evaporation. A bilayer electron-resist stack was used (MMA EL4 (90 nm) + CSAR (80 nm)) to achieve high-resolution patterns and help in the lift-off process. The nanostructures were patterned using a Raith150 e-beam writer (20 kV, 28pA, 110μC/cm^2). The sample with insulated resist was developed in 1,2-Xylene solution (1 min) followed by successive baths of propan-2-ol (1 min), DI water (1 min), and mixed propan-2-ol/DI water solution (9:1; 2 min 30 at 19.5 °C) and rinsed with Di water (1 min). Then, a 60 nm gold layer was deposited by evaporation. The lift-off was performed by immersing the samples in propan-2-one solution for 2 h. Finally, samples were rinsed in water (30 s) and dried. An O_2 plasma step (50 W, 1 min) was used to clean and remove any residual resist layer from the final structures.

Steady-State Transmission Spectrum Measurement. The optical spectra of the arrays were acquired with a customized free-space optical experimental setup. We used a stabilized tungsten-halogen light source (360−2600 nm) for the excitation, combined with an IHR 320 spectrometer (Horiba Jobin Yvon) with a UV−VIS Photomultiplier Tube (PMT) for the detection. A 1200 g/mm grating was used with 2.31 nm/mm dispersion.

Pump−Probe Spectroscopy Measurements. The transient reflectivity maps were acquired with a pump−probe spectroscopy setup already described in a previous work.[26] The laser source is a Ti:sapphire oscillator with a regenerative amplifier (Soltice, Spectra-Physics), which produces light pulses centered at 795 nm with 15 nm (FWHM) spectral width and 150 fs (FWHM) duration with a 1 kHz repetition rate. The laser source is coupled to an optical parametric amplifier (OPA 800CF, Spectra-Physics), which can tune the pump wavelength from 300 nm to 3 μm. The white light continuum probe pulse is generated by focusing the residual OPA output beam at 795 nm into a sapphire plate. Pump and probe beams are focalized on the sample by parabolic mirrors with an incidence angle of, respectively, 7.5 and −6.5° (Figure 2b). Both beams have elliptic profiles with a 1/e^2 waist radius of 88 and 93 μm for the pump and 34 and 28 μm for the probe. A motorized linear translation stage controls the delay between the pump and probe pulses over an interval up to 8 ns, with a resolution of 6.6 fs. The pump and probe duration was retrieved from the IRF (instrument response function) by measuring the two-photon absorption signal on a 150 μm BK7 microscope slide as detailed in ref 35. The reflection spectra are acquired with a CCD camera (2 × S7030-1006, Spectronic Devices Ltd). The measurements presented in Figure 3 are a mean of 10 transient maps where each point corresponds to 400 averaged measurements. The detailed data treatment is provided in the Supporting Information.

■ ASSOCIATED CONTENT

Supporting Information

The Supporting Information is available free of charge at https://pubs.acs.org/doi/10.1021/acsphotonics.2c01968.

Additional data including details of the numerical model; comparison of transient reflectivity maps (experiment and simulation); discussion of possible explanations for the differences between the experimental and numerical reflectivity temporal profiles; calculation of relative absorption within the cross and permittivity measurements of gold; and details of data processing and AFM measurements (PDF)

Video showing the temporal evolution of non-thermal electron energy density considering static non-thermal electrons (AVI)

Video showing the temporal evolution of non-thermal electron energy density considering ballistic non-thermal electrons (AVI)

Complete contact information is available at:
https://pubs.acs.org/10.1021/acsphotonics.2c01968

Author Contributions

#

J.-F.B. and M.V. were involved as major authors. They both shared the first authorship and have contributed equally to this work. M.V., P.B., J.-F.B., J.M., and M.B. have contributed to the software and simulations. J.-F.B., M.V., and P.-L.K. have done the acquisition of experimental data. The analysis and interpretation have been done by M.V., J.-F.B., P.B., J.M., and M.C. The work has been supervised by D.M., M.C., and P.C. All authors contributed to the planning of experiments. All authors contributed to the writing of the manuscript.

Funding

This work was supported by the Natural Sciences and Engineering Research Council of Canada (NSERC) with Discovery Grants for M.C. and P.G.C. A doctoral scholarship from IDEX Paris-Saclay supports M.V. This work is supported by the "ADI" project funded by the IDEX Paris-Saclay, ANR-11-IDEX-0003-02 Grant from CMC Microsystems and the MNT Financial Assistance Voucher (8774 & 10451). J-F.B. was supported by the Fonds de recherche du Québec−Nature et Technologies (FRQNT) and his Merit scholarship program for international students (no. 273433).

Notes

The authors declare no competing financial interest.
The raw transient reflection measurement dataset is available from the corresponding author upon reasonable request.

■ ACKNOWLEDGMENTS

LN2 is an International Research Laboratory (IRL) funded and co-operated by Université de Sherbrooke (UdeS), Centre National de la Recherche Scientifique (CNRS), École Centrale Lyon (ECL), Institut National des Sciences Appliquées de Lyon (INSA Lyon), and Université Grenoble Alpes (UGA). We would like to thank CMC Microsystems. We also thank Ambre Vega for providing the illustrative picture in Figure 1 and the covert art.

■ REFERENCES

(1) Hirsch, L. R.; Stafford, R. J.; Bankson, J. A.; Sershen, S. R.; Rivera, B.; Price, R. E.; et al. Nanoshell-mediated near-infrared thermal therapy of tumors under magnetic resonance guidance. *Proc. Natl. Acad. Sci.* **2003**, *100*, 13549−13554.
(2) Atwater, H. A.; Polman, A. Plasmonics for improved photovoltaic devices. *Nat. Mater.* **2010**, *9*, 205−213.
(3) Baffou, G.; Quidant, R. Nanoplasmonics for chemistry. *Chem. Soc. Rev.* **2014**, *43*, 3898.
(4) Brongersma, M. L.; Halas, N. J.; Nordlander, P. Plasmon-induced hot carrier science and technology. *Nat. Nanotechnol.* **2015**, *10*, 25−34.
(5) Qiu, J.; W ei,W .D. Surface Plasmon-Mediated Photothermal Chemistry. *J. Phys. C hem. C* **2014**, *118*, 20735−20749.
(6) Baffou, G.; Rigneault, H. Femtosecond-pulsed optical heating of gold nanoparticles. *Phys. Rev. B* **2011**, *84*, No. 035415.
(7) Inouye, H.; Tanaka, K.; Tanahashi, I.; Hirao, K. Ultrafast dynamics of nonequilibrium electrons in a gold nanoparticle system. *Phys. Rev. B* **1998**, *57*, 11334−11340.
(8) Grua, P.; Morreeuw, J. P.; Bercegol, H.; Jonusauskas, G.; Vallée, F. Electron kinetics and emission for metal nanoparticles exposed to intense laser pulses. *Phys. Rev. B* **2003**, *68*, No. 035424.
(9) Baffou, G. *Thermoplasmonics: Heating Metal Nanoparticles Using Light*. 1st ed. Cambridge University Press; 2017.
(10) Metwally, K.; Mensah, S.; Baffou, G. Fluence Threshold for Photothermal Bubble Generation Using Plasmonic Nanoparticles. *J. Phys. Chem. C* **2015**, *119*, 28586−28596.
(11) Del Fatti, N.; Voisin, C.; Achermann, M.; Tzortzakis, S.; Christofilos, D.; Vallée, F. Nonequilibrium electron dynamics in noble metals. *Phys. Rev. B* **2000**, *61*, 16956−16966.
(12) Labouret, T.; Palpant, B. Nonthermal model for ultrafast laser-induced plasma generation around a plasmonic nanorod. *Phys. Rev. B* **2016**, *94*, No. 245426.
(13) Sun, C. K.; Vallée, F.; Acioli, L. H.; Ippen, E. P.; Fujimoto, J. G. Femtosecond-tunable measurement of electron thermalization in gold. *Phys. Rev. B* **1994**, *50*, 15337−15348.
(14) Nicholls, L. H.; Stefaniuk, T.; Nasir, M. E.; Rodríguez-Fortuño, F. J.; Wurtz, G. A.; Zayats, A. V. Designer photonic dynamics by using non-uniform electron temperature distribution for on-demand all-optical switching times. *Nat. Commun.* **2019**, *10*, 2967.
(15) Schirato, A.; Crotti, G.; Proietti Zaccaria, R.; Alabastri, A.; Della, V. G. Hot carrier spatio-temporal inhomogeneities in ultrafast nanophotonics. *New J. Phys.* **2022**, *24*, No. 045001.
(16) Hopkins, P. E.; Norris, P. M. Contribution of Ballistic Electron Transport to Energy Transfer During Electron-Phonon Nonequilibrium in Thin Metal Films. *J. Heat Transfer* **2009**, *131*, No. 043208.
(17) Suslova, A.; Hassanein, A. Numerical simulation of ballistic electron dynamics and heat transport in metallic targets exposed to ultrashort laser pulse. *J. Appl. Phys.* **2018**, *124*, No. 065108.
(18) Rudenko, A.; Ladutenko, K.; Makarov, S.; Itina, T. E. Photogenerated Free Carrier-Induced Symmetry Breaking in Spherical Silicon Nanoparticle. *Adv. Opt. Mater.* **2018**, *6*, 1701153.
(19) Schirato, A.; Maiuri, M.; Toma, A.; Fugattini, S.; Proietti Zaccaria, R.; Laporta, P.; et al. Transient optical symmetry breaking for ultrafast broadband dichroism in plasmonic metasurfaces. *Nat. Photonics* **2020**, *14*, 723−727.
(20) Schirato, A.; Mazzanti, A.; Proietti Zaccaria, R.; Nordlander, P.; Alabastri, A.; Della, V. G. All-Optically Reconfigurable Plasmonic Metagrating for Ultrafast Diffraction Management. *Nano Lett.* **2021**, *21*, 1345−1351.
(21) Askes, S. H. C.; Garnett, E. C. Ultrafast Thermal Imprinting of Plasmonic Hotspots. *Adv. Mater.* **2021**, *7*, 2105192.
(22) Gargiulo, J.; Berté, R.; Li, Y.; Maier, S. A.; Cortés, E. From Optical to Chemical Hot Spots in Plasmonics. *Acc. Chem. Res.* **2019**, *52*, 2525−2535.
(23) Jack, C.; Karimullah, A. S.; Tullius, R.; Khorashad, L. K.; Rodier, M.; Fitzpatrick, B.; et al. Spatial control of chemical processes on nanostructures through nano-localized water heating. *Nat. Commun.* **2016**, *7*, 10946.
(24) Link, S.; Burda, C.; Wang, Z. L.; El-Sayed, M. A. Electron dynamics in gold and gold−silver alloy nanoparticles: The influence of a nonequilibrium electron distribution and the size dependence of the electron−phonon relaxation. *J. Chem. Phys.* **1999**, *111*, 1255−1264.
(25) Besbes, M.; Hugonin, J. P.; Lalanne, P.; van Haver, S.; Janssen, O. T. A.; Nugrowati, A. M.; et al. Numerical analysis of a slit-groove diffraction problem. *J. Eur. Opt. Soc. Rapid Publ.* **2007**, *2*, No. 07022.
(26) Bresson, P.; Bryche, J. F.; Besbes, M.; Moreau, J.; Karsenti, P. L.; Charette, P. G.; et al. Improved two-temperature modeling of ultrafast thermal and optical phenomena in continuous and nanostructured metal films. *Phys. Rev. B* **2020**, *102*, No. 155127.
(27) Pettine, J, Maioli, P, Vallee, F, Fatti, ND, Nesbitt, DJ. *Energy-Resolved Femtosecond Hot Electron Dynamics in Single Plasmonic Nanoparticles*. *30*. 2022, arxiv.

(28) Zavelani-Rossi, M.; Polli, D.; Kochtcheev, S.; Baudrion, A. L.; Béal, J.; Kumar, V.; et al. Transient Optical Response of a Single Gold Nanoantenna: The Role of Plasmon Detuning. *ACS Photonics* **2015**, *2*, 521−529.
(29) Sivan, Y.; Spector, M. Ultrafast Dynamics of Optically Induced Heat Gratings in Metals. *ACS Photonics* **2020**, *7*, 1271−1279.
(30) Block, A.; Liebel, M.; Yu, R.; Spector, M.; Sivan, Y.; García de Abajo, F. J.; et al. Tracking ultrafast hot-electron diffusion in space and time by ultrafast thermomodulation microscopy. *Sci. Adv.* **2019**, *5*, No. eaav8965.
(31) Rosei, R.; Lynch, D. W. Thermomodulation Spectra of Al, Au, and Cu. *Phys. Rev. B* **1972**, *5*, 3883−3894.
(32) Guerrisi, M.; Rosei, R.; Winsemius, P. Splitting of the interband absorption edge in Au. *Phys. Rev. B* **1975**, *12*, 557−563.
(33) Rosei, R.; Antonangeli, F.; Grassano, U. M. d bands position and width in gold from very low temperature thermomodulation measurements. *Surf. Sci.* **1973**, *37*, 689−699.
(34) Rosei, R.; Culp, C. H.; Weaver, J. H. Temperature modulation of the optical transitions involving the Fermi surface in Ag: Experimental. *Phys. Rev. B* **1974**, *10*, 484−489.
(35) Ruckebusch, C.; Sliwa, M.; Pernot, P.; de Juan, A.; Tauler, R. Comprehensive data analysis of femtosecond transient absorption spectra: A review. *J. Photochem. Photobiol., C* **2012**, *13*, 1−27.
(36) Minutella, E.; Schulz, F.; Lange, H. Excitation-Dependence of Plasmon-Induced Hot Electrons in Gold Nanoparticles. *J. Phys. Chem. Lett.* **2017**, *8*, 4925−4929.